Research Article | Vol. 32, No. 27 / 30 Dec 2024 / Optics Express 47810
Optics EXPRESS

Spatial coherence of synchrotron radiation degraded by grating monochromators

R. KHUBBUTDINOV,[1,*] G. GELONI,[2] E. SALDIN,[1] AND K. BAGSCHIK[1]

[1]Deutsches Elektronen-Synchrotron DESY, Notkestraße 85, 22607 Hamburg, Germany
[2]European XFEL, 4 Holzkoppel Street, 22869 Schenefeld, Germany
[*]ruslan.khubbutdinov@desy.de

Abstract: Fourth-generation synchrotron sources promise an enormous increase in the spatial coherence of X-ray radiation. In the EUV to soft X-ray range, the spatial coherence could reach almost 100% in both the horizontal and vertical directions. Identifying and understanding potential sources of degradation in the spatial coherence of X-rays transported along the beamline is critical to enable optimal performance for the experiments at the beamlines. Grating monochromators are an essential optical component of most EUV and soft X-ray beamlines. Recently, we have found that the spatial coherence is strongly degraded by the gratings used in these monochromators. In this work, we present a detailed physical and theoretical description of the origin and underlying effects that cause this degradation and describe the influence of the grating parameters and the exit slit of the monochromator. The theoretical analysis is presented in the framework of statistical optics. It is important to note that the described effects in the paper are distinct from the decoherence effects based on optics vibrations and the resulting virtual source broadening or wavefront degradation caused by surface irregularities and optical roughness.

1. Introduction

Spatial coherence and spectral brightness play a key role in a large number of synchrotron experiments. The demand for coherent flux for these experiments has increased enormously in recent years. Synchrotron facilities worldwide have or will upgrade their storage rings to the fourth generation (4GSR) [1–5] to meet this demand and open up new scientific opportunities. These storage rings are based on the Multi-Bend Achromat (MBA) technology and allow horizontal emittances in the order of tens of pmrad. This results in a significant increase in the spectral brightness and coherent flux of the photon sources [6,7] and enables new opportunities, in particular for coherent imaging and scattering experiments such as X-ray ptychography [8,9] and XPCS [10–13].

The increased spectral brightness of the source poses significant challenges for the beamline optics. The photon beam transport system must preserve the high spatial (transverse) coherence of the source to make it available for the actual experiment. Previous studies have investigated the spatial coherence properties of the synchrotron sources [6,7,14–17] and how they degrade due to various factors, such as optical surface defects [18–21], incoherent scattering [22,23], or vibrations of optical elements [24–26], including the Kirkpatrick-Baez (KB) system and monochromator. Depending on the number of optical components at the beamline, the effect of vibrations imposes the most significant influence on spatial coherence so far.

In the soft X-ray region, 4GSRs provide spatial coherence of almost 100% in both the horizontal and vertical directions. The spatial coherence reducing effects of the beamline optics are particularly strong here. Soft X-ray beamlines use grating monochromators to increase energy resolution. There are different types of grating monochromators, e.g. planar gratings with a downstream focusing element or self-focussing gratings such as the Varibale Line Spacing (VLS)

#542077 https://doi.org/10.1364/OE.542077
Journal © 2024 Received 25 Sep 2024; revised 4 Dec 2024; accepted 5 Dec 2024; published 16 Dec 2024

Optics EXPRESS

grating. The energy bandwidth is defined in combination with an exit slit. Studies at the soft X-ray beamline P04 at PETRA III have shown that the vertical exit slit of the monochromator affects the spatial coherence in the vertical direction [27,28]. Despite this expected effect, it has been shown that the measured spatial coherence in the dispersion direction is far below the theoretically predicted value [26,29,30]. So far, gratings have not been considered as a source of spatial coherence degradation.

In this paper, we present a physical and theoretical description for the significant degradation of the spatial coherence properties of the photon beam due to the use of grating monochromators at synchrotron facilities. We present a comprehensive study of the effect of spatial coherence degradation as a function of grating parameters under different focusing and propagation conditions. Emphasis has been placed on the spatial coherence degradation effect introduced by the grating alone, thus assuming a fully coherent incident photon beam generated by a filament source. The mathematical description and the theoretical analysis of the spatial coherence degradation are presented in the framework of statistical optics.

The first sections give an overview of the synchrotron radiation pulse structure and the mathematical description of the undulator radiation, then the basic theory of statistical optics as applied to the synchrotron source. The effect of the dispersion introduced by the grating monochromator on the spatial coherence properties of the X-ray radiation is investigated in the following sections. Individual effects of free-space propagation and focusing of the photon beam with dispersion are considered, as well as the effects of aberration and photon beam clipping by the exit slit. An evaluation of the spatial coherence properties of the photon beam and the energy resolution of the monochromator are given in these sections. The study concludes with a discussion and summary of the analysis, followed by an explanation of the effect and its applicability to synchrotron radiation sources.

2. Statistical properties of a synchrotron radiation source

This section describes the mathematical basis of the statistical methods used for synchrotron radiation (SR) sources. In order to understand the origin of spatial coherence degradation caused by gratings, it is necessary to consider the pulse structure and statistics of synchrotron radiation sources. Therefore, this section briefly discusses the pulse structure of synchrotron radiation and the mathematical description of the X-ray source, followed by the basic theory of coherence in the framework of statistical optics.

2.1. Pulse structure

In this paper an undulator is considered as the primary source of X-ray radiation. The source has an intrinsic stochastic structure driven by shot-noise statistics. This means that the fluctuations of the photon beam density are random in the six dimensional phase space volume containing two spatial, two angular, time and energy projections [6,14]. These fluctuations follow a Gaussian distribution. As a result, the produced radiation field has random amplitudes and phases, implying that the synchrotron radiation process is a Gaussian random process with shot-noise statistics imprinted in the radiation structure [14]. The latter manifests itself as longitudinal (or spectral) and transverse individual spikes in the radiation pulse. The presence of individual temporal spikes in a pulse implies the existence of certain coherent regions in the time domain with a characteristic coherence time τ_c. As such, the width of these individual spikes can be roughly estimated from the simple Fourier transform (FT) theory relations

$$\Delta\omega\Delta\tau = 2\pi, \tag{1}$$

Additionally, it was shown that the SR process is non-stationary and, consequently, non-ergodic but a quasi-stationary process [14]. In the framework of statistical optics considering quasi-stationary processes, one can estimate characteristic times of such radiation pulses by considering

Optics EXPRESS

a Wiener-Khinchin theorem [31]. According to the theorem, the coherence time of the processes with Gaussian spectral density is $\tau_c = \sqrt{\pi}/\sigma_\omega$, where σ_ω is the rms spectral width and $\Delta\omega = 2\sqrt{2ln(2)}\sigma_\omega$ is the width of the spectrum. The spectral width of the radiation produced by an undulator is [32–34]

$$\frac{\Delta\omega}{\omega} = \frac{1}{nN_u}, \tag{2}$$

where n is the harmonic number and N_u is the number of undulator periods. The typical number of periods is about $N_u = 10^2$, so that the spectral bandwidth in the soft X-ray range (500 eV - 4 keV) is about $\Delta\omega \sim 10^{16}$ Hz, and the corresponding coherence time is $\tau_c \sim 10^{-16}$ s. The characteristic duration of the electron bunch can reach values of $\sigma_t \sim 30{\cdot}10^{-12}$ s. From this, it can be seen that on the scale of pulse duration there are $N{=}\sigma_t/\tau_c{=}\ 10^5$ random intensity fluctuations or temporal spikes.

Looking at the spectral domain by analogy, one can estimate a coherent spike in the spectrum $\Delta\omega_c \sim 2\pi/\sigma_t$. In this case, the value of $\Delta\omega_c$ is about 10^{11} Hz, so the spectrum also contains about 10^5 spikes. This is shown in Fig. 1 along with the Fourier relation. As can be seen from this analysis, on the scale of the average spectrum, the coherent region (spike width) is $\Delta\omega_c/\omega_0 \approx 10^{-7}$ and rapidly disappears as one approaches the typical pulse duration of SR. Typically, today's monochromators cannot resolve a single spike, leading to the case of a convenient model for coherence analysis.

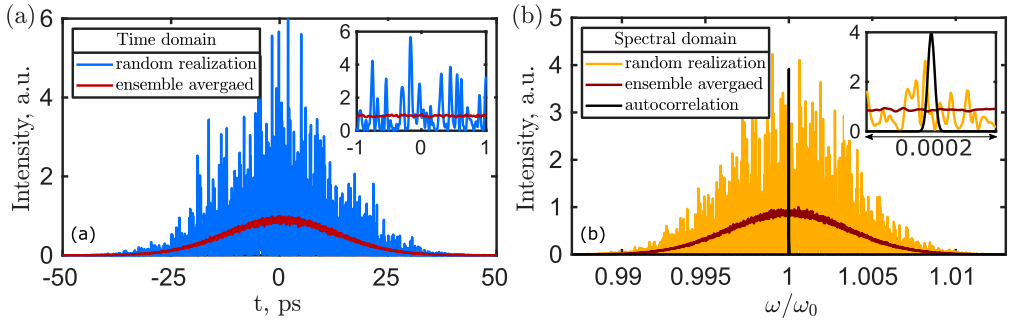

Fig. 1. Characteristic undulator radiation field in the time-frequency domain that has an intrinstic stochastic structure driven by shot-noise statistics. Gaussian intensity fluctuations of the undulator radiation in time (a) and spectral domain (b) with characteristic pulse duration $T = 30 \cdot 10^{-12}$s and coherence time $\tau_c = 1 \cdot 10^{-16}$s (a), resulting in a spectral width of $\Delta\omega/\omega \sim 0.01$ and spectral spike width $\Delta\omega_c/\omega \sim 10^{-7}$ (b). The red profile corresponds to the ensemble average of a large number of random realizations (blue). The inset shows the characteristic scale of the autocorrelation function.

2.2. *Mathematical description*

The mathematical tools of statistical optics are required to analyse the effect of spatial coherence degradation caused by gratings used in grating monochromators. For simplicity, the description and theoretical derivations are usually presented in the {**r**-ω}-domain, which implies a one-to-one correspondence to the {**r**-t}-domain via FT relations, where the following FT pair is considered for the radiation fields $E(\mathbf{r}, t)$ and $E(\mathbf{r}, \omega)$

$$E(\mathbf{r}, t) = \frac{1}{2\pi}\int_{-\infty}^{\infty} E(\mathbf{r}, \omega)e^{-i\omega t}d\omega, \tag{3}$$

$$E(\mathbf{r}, \omega) = \int_{-\infty}^{\infty} E(\mathbf{r}, t)e^{i\omega t}dt. \tag{4}$$

Optics EXPRESS

Statistical processes such as undulator radiation are treated with the concept of the statistical ensemble [31], which averages over an ensemble or many realizations of the process under consideration. In this context, the averaging is performed over the distributions of the electron bunches [14].

The radiation field $E_{k\perp}(\boldsymbol{r},\omega)$ of the kth electron can be written as a function of the deflection angle $\boldsymbol{\eta}_k$, the offset from the undulator axis $\mathbf{l}_k$ and the offset from the electron beam energy γ_k (energy spread) as [6,14]

$$E_{k\perp} = f(\boldsymbol{r},\omega,\boldsymbol{\eta}_k,\mathbf{l}_k,\gamma_k) \tag{5}$$

where $\boldsymbol{r}=\{x,y\}$ is the point of observation. The radiation field $E_{k\perp}$ considered in Eq. (5) is distributed in the transverse plane perpendicular to the electron and photon beam propagation direction at a certain distance z from the undulator center (in the far zone, considering the paraxial approximation). The total radiation field is the sum of all individual electron contributions as given by

$$E_{\perp}(\boldsymbol{r},\omega) = \sum_{k=1}^{N_e} E_{k\perp}(\boldsymbol{r},\omega,\boldsymbol{\eta}_k,\mathbf{l}_k,\gamma_k), \tag{6}$$

where N_e is the number of electrons in the beam. The parameters $\boldsymbol{\eta}_k$ and $\mathbf{l}_k$ are random variables and within the range of the electron beam divergence and size distributions. Another important random parameter t_k, the arrival time of the kth electron at the undulator entrance, must also be taken into account, as it greatly simplifies our model and the corresponding calculations when analysing spatial coherence. According to the Fourier transform in the $\{\omega,t\}$ domain in Eq. (4), applying a shift theorem to the field $E(\mathbf{r},t-t_k)$ delayed by the time t_k, there is an additional factor $e^{i\omega t_k}$ implying the transition from the $\{\mathbf{r},t\}$ to the $\{\mathbf{r},\omega\}$-domain.

The total radiation field $E(\boldsymbol{r},\omega)$ that accounts for all possible random shifts within the electron bunch is the sum of the partial contributions as given by [14]

$$E(\boldsymbol{r},\omega) = \sum_{k=1}^{N_e} E_{k\perp}(\boldsymbol{r},\omega,\boldsymbol{\eta}_k,\mathbf{l}_k,\gamma_k)e^{i\omega t_k}, \tag{7}$$

where t_k is in the range of the electron bunch duration σ_t. It is also assumed that the random arrival times t_k are independent of the random transverse shifts $\mathbf{l}_k$ and $\boldsymbol{\eta}_k$, which is the case at synchrotron facilities. In general $\boldsymbol{\eta}_k=\{\eta_x,\eta_y\}_k$, $\mathbf{l}_k=\{l_x,l_y\}_k$, γ_k and t_k are random variables following a Gaussian distribution.

The ensemble average of a function $E(a)$, where a is a random variable is defined as

$$<E(a)>= \int E(a)f(a)da. \tag{8}$$

The function $f(a)$ is the probability distribution of a. The independence of the random variables allows to write the ensemble average $<E(\boldsymbol{r},\omega)>$ as the convolution of the single electron radiation with the probability density distributions of the electron beam, over offsets f_l, deflection angles f_η, the electron beam energy f_γ and the longitudinal bunch profile f_t

$$<E(\boldsymbol{r},\omega)>= \int E_{\perp}(\boldsymbol{r},\omega,\boldsymbol{\eta},\mathbf{l},\gamma)e^{i\omega t}f_\eta(\boldsymbol{\eta})f_l(\mathbf{l})f_\gamma(\gamma)f_t(t)d\boldsymbol{\eta}d\mathbf{l}d\gamma dt. \tag{9}$$

As a result, undulator radiation can be described mathematically in terms of statistical optics by averaging over the entire volume of the phase space of random parameters [35,36].

Optics EXPRESS

2.3. Spatial coherence

The second-order coherence theory is the fundamental theory of optical coherence. It describes the correlation of electric field amplitudes [31,37,38]. The second-order correlation is described by the mutual coherence function (MCF), defined as [31]

$$\Gamma_t(\mathbf{r_1}, \mathbf{r_2}, t_1, t_2) = <E^*(\mathbf{r_1}, t_1)E(\mathbf{r_2}, t_2)>_t. \tag{10}$$

The MCF describes correlations between two electric field values $E(\mathbf{r_1}, t_1)$ and $E(\mathbf{r_2}, t_2)$ at different points in space $\mathbf{r_1}$ and $\mathbf{r_2}$ and times t_1 and t_2. The brackets $<\cdots>$ denote the time average. If the statistical process is stationary, quasi-stationary or ergodic, then the MCF can be written as a function that depends only on the time difference $\tau = t_2 - t_1$:

$$\Gamma_t(\mathbf{r_1}, \mathbf{r_2}, \tau) = <E^*(\mathbf{r_1}, t)E(\mathbf{r_2}, t + \tau)>. \tag{11}$$

In our $\{\mathbf{r}\text{-}\omega\}$-domain under consideration, the second order correlation function $\Gamma_\omega(\mathbf{r_1}, \mathbf{r_2}, \omega_1, \omega_2)$ can be written as follows

$$\Gamma_\omega(\mathbf{r_1}, \mathbf{r_2}, \omega_1, \omega_2) = <E^*(\mathbf{r_1}, \omega_1)E(\mathbf{r_2}, \omega_2)>, \tag{12}$$

where functions $\Gamma_t(\mathbf{r_1}, \mathbf{r_2}, t_1, t_2)$ and $\Gamma_\omega(\mathbf{r_1}, \mathbf{r_2}, \omega_1, \omega_2)$ form a Fourier pair

$$\Gamma_t(\mathbf{r_1}, \mathbf{r_2}, t_1, t_2) = \frac{1}{4\pi^2}\int_{-\infty}^{\infty}\Gamma_\omega(\mathbf{r_1}, \mathbf{r_2}, \omega_1, \omega_2)e^{i\omega_1 t_1}e^{-i\omega_2 t_2}d\omega_1 d\omega_2. \tag{13}$$

Taking into account the properties of synchrotron radiation described above, the second-order correlation function in the $\{\mathbf{r}\text{-}\omega\}$-domain can be split in the product of a spectral and a spatial factors [14]

$$\Gamma_\omega(\mathbf{r_1}, \mathbf{r_2}, \omega_1, \omega_2) = G_\omega(\omega_1 - \omega_2)G_\perp(\mathbf{r_1}, \mathbf{r_2}), \tag{14}$$

where $G_\omega(\omega_1 - \omega_2)$ is the spectral correlation function which can be approximated by Dirac δ-function $\delta(\omega_1 - \omega_2)$ [31], and $G_\perp(\mathbf{r_1}, \mathbf{r_2}, \omega_1)$ is the cross-spectral density function (CSD) [31], which describes spatial correlations. From now on we will be concerned with the calculation of the cross-spectral density $G_\perp(\mathbf{r_1}, \mathbf{r_2})$, where the frequency argument of the function is omitted and the quasi-monochromatic approximation is considered. Using the mathematical description of the undulator source presented in section 2.2, the CSD function [14] is given by

$$G_\perp(\mathbf{r_1}, \mathbf{r_2}) = \frac{1}{2\pi}\int_{-\infty}^{\infty} d\Delta\omega\, E^*(\mathbf{r_1}, \Delta\omega)E(\mathbf{r_2}, \Delta\omega). \tag{15}$$

The fact that each monochromator has an intrinsically limited resolving power was taken into account in the derivation of Eq. (15) [14]. It is necessary to introduce a quantity for $G_\perp(\mathbf{r_1}, \mathbf{r_2})$ that represents its efficiency. This quantity is the degree of transverse coherence (DoTC) ζ, which characterises the spatial coherence of synchrotron radiation by a single number [14,31] and is described by

$$\zeta = \frac{\int_{-\infty}^{\infty}\int_{-\infty}^{\infty} d\mathbf{r_1}d\mathbf{r_2}\,|G_\perp(\mathbf{r_1}, \mathbf{r_2})|^2}{\left|\int_{-\infty}^{\infty} d\mathbf{r}\, G_\perp(\mathbf{r}, \mathbf{r})\right|^2}. \tag{16}$$

3. Grating dispersion and spatial coherence degradation

The spatial coherence properties of the photon beam after interaction with a grating are described in detail in this section. The assumptions and simplifications of the previous sections are adopted. The most important simplification is the factorisation of the spatial and spectral components of the incident field amplitude. In addition, a fully coherent incident photon beam with a Gaussian

Optics EXPRESS

spatial distribution is assumed. The influence of grating dispersion on spatial coherence is studied both for free space propagation and for focusing. The influence of aberrations in the focusing of the photon beam together with the grating dispersion is analysed in the following part. The variation of the spatial coherence properties of the photon beam as a function of the energy resolution of the grating monochromator is analysed in the last section.

3.1. Free-space propagation

It has been shown that undulator radiation follows the same Gaussian random statistics as thermal light [14]. However, unlike thermal sources, which are completely incoherent, undulator sources are partially coherent, with a coherent spot size equal to the single-electron diffraction size. From the sections 2.2 (Eq. (9)) and 2.3 (Eq. (10)) it can be seen that the partial coherence of the undulator source is determined by the randomly distributed parameters $\boldsymbol{\eta}$, $\mathbf{l}$, γ of the electron beam.

The analysis presented here is limited to the effects associated with the grating. Effects associated with the random spatial and angular distribution of the electron beam are not considered, which assumes complete spatial coherence of the photon beam incident on the grating. As such, the photon beam incident on the grating with a given carrier frequency ω_0 can be written as

$$E_i(\mathbf{r}, t) = E_i(t)E_i(\mathbf{r})e^{-i\omega_0 t}, \tag{17}$$

where we assumed that the temporal $E(t)$ and the spatial $E(\mathbf{r})$ components of the incident field amplitude $E_i(\mathbf{r}, t)$ can be separated.

In the following, only the one-dimensional spatial case is considered, in which the incident photon beam has the geometry shown in Fig. 2(a).

$$E_i(x, t) = E_i(t)E_i(x)e^{-i\omega_0 t}. \tag{18}$$

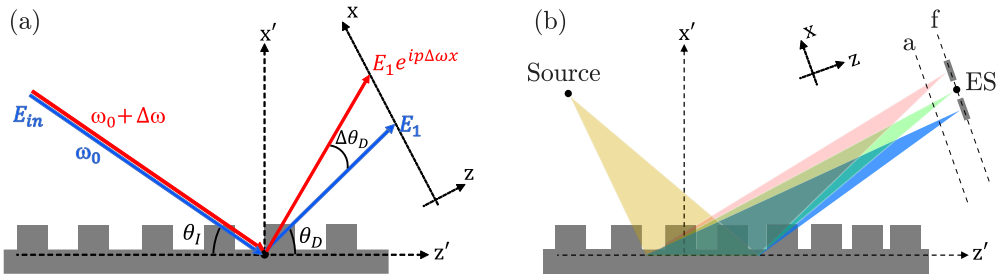

Fig. 2. (a) Schematic of a plane grating. A photon beam with a frequency offset $\Delta\omega$ (red) from the carrier frequency ω_0 (blue) exhibits an additional phase term, which depends on the specifications of the grating. (b) Schematic of a VLS grating. The polychromatic photon beam from the source is spectrally separated and focused by the VLS grating to the focal plane f at the ES position. To calculate defocus aberrations, the ES is placed out of focus at position a. Please note that all distances and angles in (a) and (b) are exaggerated. The spatial characteristics are considered in the x-plane, which is perpendicular to the propagation.

The electric field amplitude in the corresponding $\{x, \omega\}$ domain according to Eq. (4) has the form

$$E_i(x, \Delta\omega) = \int_{-\infty}^{\infty} dt\, E_i(t)E_i(x)e^{-i\omega_0 t}e^{i\omega t} = E_i(\Delta\omega)E_i(x), \tag{19}$$

where $\Delta\omega = \omega - \omega_0$.

Optics EXPRESS

An incident electric field with Gaussian spatial and spectral distributions, characterised by their rms widths σ_{x_0} and σ_ω respectively, has been considered for the following calculations. The Gaussian distributions are described by

$$E_i(x) = exp\left[-\frac{x^2}{2\sigma_{x_0}^2} \right], \tag{20}$$

$$|E_i(\Delta\omega)|^2 = exp\left[-\frac{\Delta\omega^2}{2\sigma_\omega^2} \right]. \tag{21}$$

Note that in Eq. (20) the amplitude of the incident electric field and in Eq. (21) the intensity of the field spectrum are considered.

In the following, the Gaussian distributions described in Eqs. (20) and (21) are used to simplify the functional form of the CSD function. In this case, $E_i(\Delta\omega)$ can be considered as the ensemble average of the spectrum. The use of simple amplitude forms is sufficient for a quantitative analysis of the problem. According to Eq. (15), upon using the following definitions

$$\begin{aligned} x_1 &= \bar{x} + \frac{\Delta x}{2} \\ x_2 &= \bar{x} - \frac{\Delta x}{2} \end{aligned} \tag{22}$$

the CSD of the electric field between points x_1 and x_2 can be defined in full generality (see Supplement 1) by

$$G_\perp(\bar{x}, \Delta x) = \frac{1}{2\pi} \int_{-\infty}^{\infty} d\Delta\omega\, E^* \left(\bar{x} + \frac{\Delta x}{2}, \Delta\omega \right) E \left(\bar{x} - \frac{\Delta x}{2}, \Delta\omega \right) . \tag{23}$$

The DoTC is accordingly described by

$$\zeta = \frac{\int_{-\infty}^{\infty} \int_{-\infty}^{\infty} d\bar{x}\, d\Delta x\ |G_\perp(\bar{x}, \Delta x)|^2}{\left| \int_{-\infty}^{\infty} d\bar{x}\, G_\perp(\bar{x}, \Delta x = 0) \right|^2} . \tag{24}$$

As already mentioned, we assume full spatial coherence of the beam incident on the grating, which can be seen by the substitution of $E_i(x, \Delta\omega) = E_i(x)E_i(\Delta\omega)$ in Eq. (23) and Eq. (24)

$$G_\perp(\bar{x}, \Delta x) = \frac{1}{2\pi} \int_{-\infty}^{\infty} d\Delta\omega\, exp\left[-\frac{(\bar{x} + \frac{\Delta x}{2})^2}{2\sigma_{x_0}^2} \right] exp\left[-\frac{(\bar{x} - \frac{\Delta x}{2})^2}{2\sigma_{x_0}^2} \right] exp\left[-\frac{\Delta\omega^2}{2\sigma_\omega^2} \right], \tag{25}$$

$$\zeta = \frac{\int_{-\infty}^{\infty} \int_{-\infty}^{\infty} dx_1 dx_2\, |G_{i\perp}(\bar{x}, \Delta x)|^2}{\left| \int_{-\infty}^{\infty} dx\, G_{i\perp}(\bar{x}, \Delta x = 0) \right|^2} = 1 . \tag{26}$$

The CSD in Eq. (25) is obtained by integrating over all individual frequencies within the incident energy bandwidth. It shows that the photon beam incident on the grating, which is characterised by Gaussian spatial and spectral distributions, has a degree of transverse coherence $\zeta = 1$ and is therefore fully spatially coherent.

An electric field incident on the grating with an energy offset $\hbar\Delta\omega$ from the resonant energy $\hbar\omega_0$ results in an angular increment, as shown in Fig. 2(a). As a result, it acquires an additional

Optics EXPRESS

phase term in the $\{x, \Delta\omega\}$ domain (see Supplement 1),

$$E_g(x, \Delta\omega) = E(x, \Delta\omega)e^{ip\Delta\omega x}, \tag{27}$$

where $p{=}\Delta k_x/\Delta\omega$ is the dispersion parameter of the grating. The photon beam directly after the grating according to Eq. (27) is described by

$$E_g(x, \Delta\omega) = exp\left[-\frac{x^2}{2\sigma_x^2} \right] E_i(\Delta\omega)e^{ip\Delta\omega x}, \tag{28}$$

where the photon beam width $\sigma_x = \frac{\theta_D}{\theta_I}\sigma_{x_0}$ is corrected for the "astigmatism" factor due to the difference in exit and entrance angles. In Eq. (28), the diffracted electric field of each individual frequency $\Delta\omega$ contains a phase term with a certain tilt proportional to $\Delta\omega$ and p, with the exception of the carrier (resonant) frequency ω_0. The tilt implies that the spatial and frequency components of the electric field are coupled. The amplitude and phase distribution of the spatial part of the electric field directly after the grating is shown in Fig. 3(a) for three different energies. It shows that the photon beams strongly overlap spatially. However, the phase profiles of the individual photon beams are tilted with respect to the carrier (resonant) frequency (ω_0).

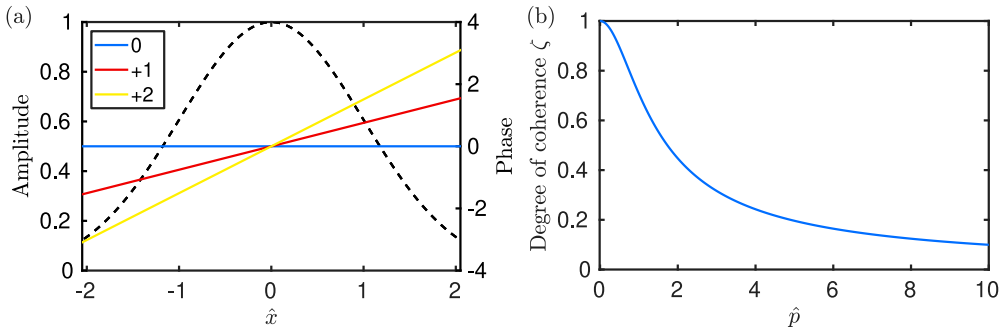

Fig. 3. (a) Amplitude and phase distributions of the spatial part of the photon beam directly after the grating for three different frequencies (energies). The blue line corresponds to the phase distribution of the central frequency ω_0 (e.g., 1200 eV), the red line for the frequency offset $\Delta\omega/\omega_0 = +1{\cdot}10^{-5}$ (1200.01 eV) and the yellow line for the frequency offset $\Delta\omega/\omega_0 = +2{\cdot}10^{-5}$ (1200.02 eV). The black dashed line corresponds to the amplitude distribution of the photon beam including all three frequencies. The horizontal $\hat{x}$-axis is normalized to the size of the beam σ_x. (b) DoTC of the photon beam direcly after the grating as a function of the normalised dispersion parameter $\hat{p}$ (see Eq. (30)).

Substitution of Eq. (28) into Eq. (23) gives the expression for the CSD of the photon beam after the grating

$$G_{g\perp}(\bar{x}, \Delta x) = \frac{1}{\sqrt{2\pi}}\sigma_\omega \exp\left[-\frac{\sigma_\omega^2 p^2 (\Delta x)^2}{2} \right] \exp\left[-\frac{\bar{x}^2 + (\Delta x)^2/4}{\sigma_x^2} \right]. \tag{29}$$

Further Substitution of the expression (Eq. (29)) into Eq. (24) gives the DoTC

$$\zeta_g = \frac{1}{\sqrt{1 + 2p^2\sigma_\omega^2\sigma_x^2}} = \frac{1}{\sqrt{1 + \hat{p}^2}}, \tag{30}$$

where $\hat{p} = \sqrt{2}\sigma_\omega\sigma_x p$ is the normalised dispersion parameter. Equation (30) shows that the degree of transverse coherence is unity (full spatial coherence) for a monochromatic beam $\sigma_\omega = 0$. The

Optics EXPRESS

degree of transverse coherence as a function of the normalised dispersion parameter is shown in Fig. 3(b). It can be seen that with increasing $\hat{p}$, the spatial coherence of the photon beam decreases significantly. The increase of $\hat{p}$ can be caused either by an increase of the incident energy bandwidth $\hbar\sigma_\omega$, the photon beam footprint on the grating σ_x/θ_D, or the dispersion parameter p.

Replacing the dispersion parameter p by the grating parameters (see Supplement 1), the degree of transverse coherence of the photon beam directly after the grating (assuming diffraction in the first order) is described by

$$\zeta_g = \frac{1}{\sqrt{1 + \frac{2\lambda^2\sigma_\omega^2\sigma_x^2}{d^2c^2\theta_D^2}}}, \tag{31}$$

where d is the groove spacing of the grating, c is the speed of light and λ is the wavelength corresponding to the carrier (resonant) frequency ω_0.

In the framework of Gaussian-Schell Model (GSM) [31,39] the CSD function G_{GSM} is defined as follows

$$G_{GSM}(\bar{x}, \Delta x) = \sqrt{G_\perp(\bar{x} + \Delta x/2, 0)}\sqrt{G_\perp(\bar{x} - \Delta x/2, 0)} exp\left(-\frac{(\Delta x)^2}{L_g^2}\right). \tag{32}$$

By comparing Eq. (29) and Eq. (32) one can estimate the spatial coherence length of the diffracted field immidiately after the grating in the framework of GSM

$$L_g = \frac{1}{\sigma_\omega p}. \tag{33}$$

In Eq. (33) it can be seen that the spatial coherence length depends only on the incoming bandwidth σ_ω and the grating parameter p.

In the following, the propagation of the diffracted electric field after the grating and its spatial coherence properties will be discussed. In this case, a slowly varying envelope of the field with respect to the frequency is assumed, as described by $E(x, z, \Delta\omega) = E_g(x, z_0, \Delta\omega)\exp(-i\omega z/c)$. The propagation of the diffracted field $E_g(x', \Delta\omega)$ in free-space up to a distance z is given by the propagator

$$P_z(x - x') = \sqrt{\frac{i\omega_0}{2\pi cz}} exp\left[\frac{i\omega_0(x - x')^2}{2cz}\right], \tag{34}$$

and is defined as

$$\begin{aligned} E_z(x, \Delta\omega) &= \int_{-\infty}^{\infty} E_g(x', \Delta\omega) P_z(x - x') dx' \\ &= E_0 exp\left[\frac{ix^2/\sigma_x - p^2\Delta\omega^2\sigma_x\hat{z} + 2xp\Delta\omega\sigma_x}{2(\hat{z} - i\sigma_x)}\right] \end{aligned} \tag{35}$$

where E_0 contains all non-essential pre-integral factors, and $\hat{z}$ is defined as

$$\hat{z} = \frac{cz}{\omega_0\sigma_x}. \tag{36}$$

In Eq. (35) a narrow bandwidth $\Delta\omega$ around ω_0 is assumed. This assumption is valid until $\Delta\omega x^2/(cz) \ll 1$, otherwise we cannot consider the frequency $\omega = \omega_0$ fixed anymore. Substitution

Optics EXPRESS

of the propagator (Eq. (35)) into Eq. (23) gives CSD function

$$G_{z\perp}(\bar{x}, \Delta x) = G_{z_0} exp\left[\frac{i\hat{z}\bar{x}\Delta x/\sigma_x - \bar{x}^2/\widetilde{p} - (\Delta x/2)^2}{\hat{z}^2 + \sigma_x^2/\widetilde{p}}\right], \tag{37}$$

where the new parameter $\widetilde{p}$ is defined as

$$\widetilde{p} = 1 + 2p^2\sigma_x^2\sigma_\omega^2 = 1 + \hat{p}^2. \tag{38}$$

Interestingly, substitution of CSD (Eq. (37)) into Eq. (24) gives exactly the same expression as in Eq. (30) for DoTC directly after the grating $\zeta_z = \zeta_g$. This means that the degree of transverse coherence of the photon beam is preserved as it propagates in free-space after diffraction by the grating. However the coherence length of the beam now depending on the distance z from the grating and can be estimated from Eq. (37) in the framework of Gaussian-Schell Model [31,39]

$$L_z = L_g\sqrt{\hat{z}^2/\sigma_x^2 + 2\hat{z}^2/L_g^2 + 1}. \tag{39}$$

For $z \to 0$, the coherence length is equal to the coherence length immediately behind the grating $L_z = L_g$.

3.2. Influence of focusing

For efficient monochromization, the photon beam diffracted by the grating is focused into the plane of the exit slit aperture. Focusing can be achieved by using an additional focusing element after a plane grating or by using a self-focusing grating such as a Variable Line Spacing (VLS) grating (as shown in Fig. 2(b)). The latter is used in the following to describe the spatial coherence properties of the photon beam upon focusing.

To simplify the mathematical description of a VLS grating, it can be represented by a plane grating in conjunction with a 'virtual lens' [40,41]. This is sufficient for a qualitative analysis of the spatial coherence properties of a VLS grating. The approach simplifies the expressions for the diffracted field $E_g(x', \Delta\omega)$ and the CSD $G_{g\perp}(\bar{x}, \Delta x)$. The virtual lens is mathematically described by the following transmission function

$$T_f(x, \omega_0) = exp\left[\frac{-i\omega_0 x^2}{2cf}\right], \tag{40}$$

where f is the focal length of the VLS grating. Using a propagator (Eq. (34)), the electric field $E_f(x, \Delta\omega)$ in the focal plane of the virtual lens is described by

$$\begin{aligned} E_f(x, \Delta\omega) &= \sqrt{\frac{i\omega_0}{2\pi cf}}\int_{-\infty}^{\infty} E_g(x', \Delta\omega) exp\left[\frac{-i\omega_0 x'^2}{2cf}\right] exp\left[\frac{i\omega_0(x-x')^2}{2cf}\right] dx' \\ &= \sqrt{\frac{i\sigma_x}{\sigma_f}} exp\left[\frac{-\Delta\omega^2}{4\sigma_\omega^2}\right] exp\left[\frac{i\omega_0 x^2}{2cf}\right] exp\left[\frac{-x^2}{2\sigma_f^2}\right] exp\left[\frac{-p^2\Delta\omega^2\sigma_x^2}{2}\right] exp\left[\frac{p\Delta\omega x\sigma_x}{\sigma_f}\right], \end{aligned} \tag{41}$$

where the width of the focused monochromatic beam σ_f is defined by

$$\sigma_f = \frac{fc}{\omega_0\sigma_x}. \tag{42}$$

Note that the expression in Eq. (42) is only valid for 1:1 focusing.

The amplitude and phase distribution of the spatial part of the photon beam at the exit slit plane is shown in Fig. 4 for three different energies. In contrary to the case of free-space

Optics EXPRESS

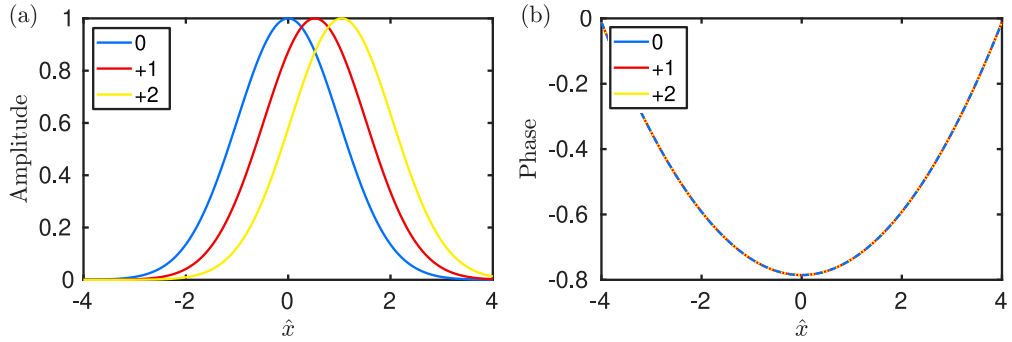

Fig. 4. Amplitude and phase distributions of the spatial part of the photon beam at the exit slit plane for three different frequencies (energies). The blue line corresponds to the phase and amplitude distribution of the central frequency ω_0 (e.g., 1200 eV), the red line for the frequency offset $\Delta\omega/\omega_0 = +1{\cdot}10^{-5}$ (1200.01 eV) and the yellow line for the frequency offset $\Delta\omega/\omega_0 = +2{\cdot}10^{-5}$ (1200.02 eV). The horizontal $\hat{x}$-axis is normalized to the size of the focused monochromatic beam σ_f.

propagation (see Fig. 3(a)), the phase distribution for the different energies is equal. However, the amplitude distribution of these photon beams are spectrally seperated. The degree of separation is determined by the dispersion parameter p.

Substitution of Eq. (41) into Eq. (23) gives the expression for the CSD of the photon beam at the focal plane

$$G_{f\perp}(\bar{x}, \Delta x) = G_{f_0} exp\left[-\frac{i\bar{x}\Delta x}{\sigma_f \sigma_x} \right] exp\left(-\frac{[\bar{x}^2/\widetilde{p} + (\Delta x/2)^2]}{\sigma_f^2} \right). \tag{43}$$

Suprisingly, further substitution of the expression (Eq. (43)) into Eq. (24) gives the same expression as for the degree of transverse coherence directly after the grating (Eq. (30)) and during propagation $\zeta_f = \zeta_z = \zeta_g$ although the amplitude and phase distributions are different in both cases. This implies that the degree of spatial coherence of the photon beam does not change upon propagation or focusing and is hence preserved. Note that the result is the same if a plane grating is used in conjuction with a focusing mirror instead of a VLS grating. Similar to the previous calculations, the coherence length of the beam in the focus can be estimated from the CSD function in Eq. (43)

$$L_f = L_g \sqrt{\sigma_f^2/\sigma_x^2 + 2\sigma_f^2/L_g^2}. \tag{44}$$

3.3. Defocus aberration

The following section describes the effect of defocus aberration on the spatial coherence properties of the photon beam after the grating. It is assumed that the defocus aberration has the largest effect on the beam properties. All other aberrations are neglected for simplicity.

Defocus aberration is implemented by an additional phase factor

$$P_a(x) = exp\left[\frac{iax^2}{\sigma_x^2} \right]. \tag{45}$$

Optics EXPRESS

Such aberrations can be considered in the out-of-focus plane, as shown in Fig. 2(b). Substitution of Eq. (45) into Eq. (41) gives the expression for the diffracted electric field with defocus aberration

$$\begin{aligned} E_f^a(x,\Delta\omega) &= \sqrt{\frac{i\omega_0}{2\pi cf}}\int_{-\infty}^{\infty} E_g(x',\Delta\omega)exp\left[\frac{-i\omega_0 x'^2}{2cf}\right]P_a(x')exp\left[\frac{i\omega_0(x-x')^2}{2cf}\right]dx' \\ &= E_0^a exp\left[\frac{-\Delta\omega^2}{4\sigma_\omega^2}\right]exp\left[\frac{i\omega_0 x^2}{2cf}\right]exp\left[\frac{1}{(1-2ia)}\left(\frac{-x^2}{2\sigma_f^2}-\frac{p^2\Delta\omega^2\sigma_x^2}{2}+\frac{p\Delta\omega x\sigma_x}{\sigma_f}\right)\right]. \end{aligned} \tag{46}$$

The CSD function $G_{f\perp}^a(\bar{x},\Delta x)$ in the exit slit plane including defocus aberration is obtained by substitution of Eq. (46) into Eq. (23)

$$G_{f\perp}^a(\bar{x},\Delta x) = G_{a_0}exp\left[\frac{-i\bar{x}\Delta x}{\sigma_f\sigma_x}\right]exp\left(\frac{2ia\bar{x}\Delta x-\bar{x}^2-(\Delta x/2)^2\widetilde{p}}{\sigma_f^2(4a^2+\widetilde{p})}\right). \tag{47}$$

For $a \to 0$, the CSD function $G_{f\perp}^a(\bar{x},\Delta x) = G_{f\perp}(\bar{x},\Delta x)$. The degree of transverse coherence ζ^a including defocus aberration is obtained by subtituting Eq. (47) into Eq. (24) which gives the same expression as in Eq. (30) (ζ^a=ζ_g), which is expected since DoTC does not change upon focusing or propagation. It confirms that the spatial coherence properties of the photon beam is preserved upon propagation and focusing which includes defocus aberration. Coherence length in the case of defocus aberration is obtained from the equation Eq. (47) by the analogy with the previous calculations

$$L_a = L_g\sqrt{\sigma_f^2/\sigma_x^2 + 2\sigma_f^2/L_g^2 + 4a^2/\sigma_x^2}. \tag{48}$$

For $a \to 0$, the coherence length is equal to the coherence length in the focus $L_a = L_f$.

3.4. Exit slit aperture and energy resolution

The exit slit aperture is an integral part of a grating monochromator. It selects a certain spectral bandwidth of the incident photon beam and thus defines the resolving power of the monochromator. At the same time, it acts as a spatial filter and affects the spatial coherence properties of the monochromator. The effect of the exit slit aperture and its size on the spatial coherence properties of the photon beam is described below. Mathematically, the transmission function of the exit slit aperture can be approximated by a Gaussian function given by

$$T_s(x) = exp(-\frac{x^2}{2\sigma_s^2}), \tag{49}$$

where σ_s is the root mean square of the slit amplitude function. Note that the exit slit size is the FWHM of $T_s(x)$. The intensity of the photon beam after the exit slit is defined as

$$\begin{aligned} I_{es}(\Delta\omega) &= \left|\int_{-\infty}^{\infty} E_f(x,\Delta\omega)T_s(x)dx\right|^2 \\ &= \frac{2\pi\sigma_f\sigma_x}{\sigma_s\sqrt{\sigma_f^2/\sigma_x^2+(\sigma_f^2/\sigma_s^2+1)^2}}exp\left[-\frac{\Delta\omega^2}{2\sigma_{res}^2}\right], \end{aligned} \tag{50}$$

where σ_{res} is the energy resolution of the monochromator that include incoming and transmitted bandwidth

$$\sigma_{res} = \frac{1}{\sqrt{1/\sigma_\omega^2 + 1/\sigma_{\omega s}^2}}. \tag{51}$$

Optics EXPRESS

In Eq. (51), the energy resoultion $\sigma_{\omega s}$ related to the exit slit aperture (transmitted bandwidth) is defined as

$$\sigma_{\omega s} = \frac{1}{\sqrt{2\sigma_x^2 p^2}} \left[\left(1 + \frac{\sigma_s^2}{\sigma_f^2}\right)^2 + \frac{\sigma_s^4}{\sigma_f^2 \sigma_x^2} \right]^{\frac{1}{2}} \left[1 + \frac{\sigma_s^2}{\sigma_f^2} \left(1 + \frac{\sigma_s^2}{\sigma_x^2}\right) \right]^{-\frac{1}{2}}. \tag{52}$$

If the exit slit aperture is fully closed $\sigma_s \to 0$, the normalised energy resolution is given by

$$\frac{\sigma_{\omega s}}{\omega_0} = \frac{1}{\sqrt{2\sigma_x^2 p^2 \omega_0^2}} = \frac{1}{\sqrt{2\sigma_x^2 \frac{4\pi^2}{\omega_0^2 d^2 \theta_D^2} \omega_0^2}} = \frac{1}{\pi \frac{2\sqrt{2}\sigma_x}{\theta_D d}} \approx \frac{1}{\pi \frac{\Delta x_f}{d}} = \frac{1}{\pi N_g}, \tag{53}$$

where $\Delta x_f \approx 2\sqrt{2}\sigma_x/\theta_D$ (FWHM) is the footprint of the incident photon beam on the grating and $\Delta x_f/d = N_g$ is the number of illuminated grooves. In this case, the energy resolution of the monochromator is only determined by the total number of illuminated grooves. The maximum energy resolution σ_{res} ($\sigma_s \to 0$) that can be obtained is described by

$$\sigma_{res} = \frac{\sigma_\omega}{\sqrt{1 + 2p^2\sigma_x^2\sigma_\omega^2}} = \frac{1}{\sqrt{1 + \hat{p}^2}} = \frac{\sigma_\omega}{\sqrt{\hat{p}}}. \tag{54}$$

The resolving power of the monochromator ω_0/σ_{res} as a function of σ_s for different dispersion parameters $\hat{p}$ is shown in Fig. 5(a). It can be seen that the resolving power increases as expected with decreasing σ_s compared to σ_f. By increasing the dispersion parameter $\hat{p}$, the separation of the individual photon beams of different energies increases, resulting in an increasing resolving power for a given exit slit aperture size.

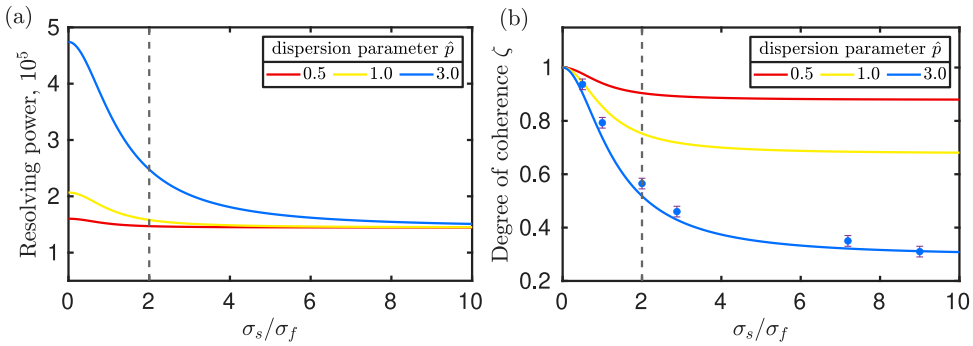

Fig. 5. (a) Grating resolving power (ω_0/σ_{res}, see Eq. (51)) and (b) DoTC (see Eq. (57)) as a function of the ratio of the exit slit size σ_s and the size of the focused monochromatic beam σ_f after the ES for different dispersion parameters $\hat{p}$. The blue circles show the results of wave-optical simulations carried out with the Xrt software [42].

According to [38], the CSD function $G_{s\perp}(x_1, x_2)$ directly after the exit slit aperture is defined as

$$G_{s\perp}(x_1, x_2) = T_s^*(x_1) T_s(x_2) G_{f\perp}(x_1, x_2), \tag{55}$$

and in the $\bar{x}, \Delta x$-domain by

$$G_{s\perp}(\bar{x}, \Delta x) = \frac{\sigma_\omega \sigma_x}{\sqrt{2\pi}\sigma_f} exp\left[\frac{-i\bar{x}\Delta x}{\sigma_f \sigma_x}\right] exp\left[\bar{x}^2 \left(\frac{1}{\sigma_f^2 \tilde{p}} - \frac{1}{\sigma_s^2}\right) - \left(\frac{\Delta x}{2}\right)^2 \left(\frac{1}{\sigma_f^2} + \frac{1}{\sigma_s^2}\right)\right]. \tag{56}$$

Optics EXPRESS

The DoTC directly after the exit slit is given by

$$\zeta_{es} = \sqrt{\frac{\sigma_s^2/(\sigma_f^2\widetilde{p}) + 1}{\sigma_s^2/\sigma_f^2 + 1}}. \tag{57}$$

Figure 5(b) shows the DoTC as a function of the rms exit slit aperture size σ_s for different dispersion parameters $\hat{p}$. It can be seen that the degree of transverse coherence approaches unity as expected with decreasing σ_s compared to σ_f. However, as can be seen from Eq. (57), in order to obtain 100% of spatial coherence in this case, the exit slit should be completely closed, which does not make much sense since there is no flux available afterward. On the other hand, increasing $\hat{p}$ for a given σ_s, significantly decreases the DoTC ζ_{es}. This is the opposite behaviour to the effect on the resolving power. As a result, the condition for the highest resolving power of the monochromator is accompanied by the lowest spatial coherence properties (for instance compare values for the slit openning of $2\sigma_f$ for the same dispersion parameter $\hat{p}$, vertical dashed line Fig. 5(a,b)). Note that the calculations assume 1:1 focusing without defocus aberration. It should also be noted that σ_f is the effective size of the focused monochromatic photon beam, while the total photon beam size at the exit slit plane is proportional to its spectral bandwidth.

To support the theoretical calculations, additional wave-optical simulations were performed using the Xrt [42] software. The results of the simulations, for the case of $\hat{p}$=3, are shown in Fig. 5(b). It can be seen that the results of the wave-optical simulations are in good agreement with the theoretical calculation. However, slight variations are observed due to different implementations of the exit slit in the Xrt software (sharp-edged slit) and theoretical calculations (Gaussian slit). There is no difference between the DoTC obtained from the simulations and the theoretical calculations when the opening of the ES is larger than the size of the incident beam. The DoTC from the simulation is determined by the mode decomposition method [7,31]. The statistical error of the simulations is ≈ 2 % [7].

The effect of the exit slit aperture on the spatial coherence properties of the diffracted photon beam, including defocus aberration, is described below. Defocus aberration results in a translation of the focus along the optical axis out of the exit slit plane. Consequently, the size of the photon beam at the exit slit aperture is increased. The intensity distribution of the photon beam after the exit slit aperture is, in analogy to Eq. (50), given by

$$\begin{aligned} I_{es}^a(\Delta\omega) &= \left| \int_{-\infty}^{\infty} E_f^a(x,\Delta\omega) T_s(x) dx \right|^2 \\ &= \frac{2\pi\sigma_f\sigma_s^2}{\sqrt{(1+4a^2)(1/\sigma_x^2+\sigma_f^2/\sigma_s^2)+4(1-2a/\sigma_x\sigma_s+1/\sigma_s^2)}} exp\left[-\frac{\Delta\omega^2}{2\sigma_{res}^2}\right], \end{aligned} \tag{58}$$

and the bandpass $\sigma_{\omega s}$ related to the exit slit aperture size is defined as

$$\begin{aligned} \sigma_{\omega s} = &\frac{1}{\sqrt{2\sigma_x^2 p^2}} \left[1 + \frac{\sigma_s^2}{\sigma_f^2}\left(1 + \frac{\sigma_s^2}{\sigma_x^2}\right)\right]^{-\frac{1}{2}} \\ &\times \left[\left(1+\frac{\sigma_s^2}{\sigma_f^2}\right)^2 + \frac{\sigma_s^4}{\sigma_f^2\sigma_x^2} + 4a\left(a + a\frac{\sigma_s^4}{\sigma_x^2\sigma_f^2} - \frac{\sigma_s^4}{\sigma_f^3\sigma_x}\right)\right]^{\frac{1}{2}}. \end{aligned} \tag{59}$$

Note, that the expression in Eq. (59) takes the form of Eq. (52) for ($a \to 0$).

The resolving power for different grating settings is shown in Fig. 6(a). It can be seen that, for a given exit slit aperture and dispersion parameter $\hat{p}$, the resolving power decreases significantly with increasing defocus aberration. The reason for this is the decreasing spatial separation of the

Optics EXPRESS

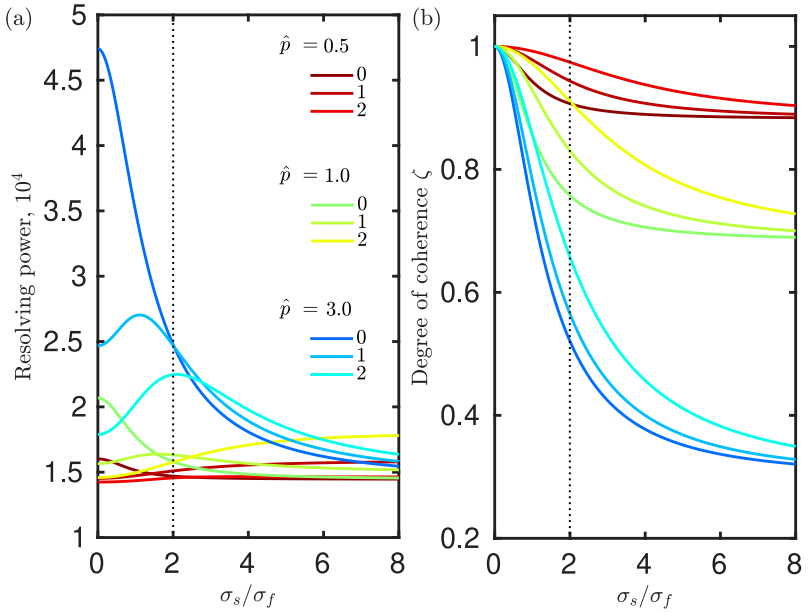

Fig. 6. (a) Grating resolving power (ω_0/σ_{res}, see Eq. (51) and Eq. (59)) as a function of the ratio of the exit slit size σ_s and the size of the focused monochromatic beam σ_f after the ES for different dispersion parameters $\hat{p}$ and defocus aberrations a. (b) DoTC as a function of the relation between the exit slit size σ_s and the size of the focused monochromatic beam σ_f after the ES for different dispersion parameters $\hat{p}$ and defocus aberrations a (see Eq. (60)). The ES is placed out of focus for the calculations (see Fig. 2(b)).

photon beams of individual energies out of focus illuminating the exit slit aperture. For large exit slit sizes or small focus sizes, the effect of aberration is less pronounced.

The CSD function of the photon beam directly after the exit slit aperture is defined according to Eq. (55) and the DoTC according to Eq. (24) which is given by

$$\zeta_{es}^{a} = \sqrt{\frac{\sigma_s^2/\sigma_f^2 + \widetilde{p} + 4a^2}{\widetilde{p}(\sigma_s^2/\sigma_f^2 + 1) + 4a^2}}. \tag{60}$$

The degree of transverse coherence for different grating settings is shown in Fig. 6(b). It can be seen that the spatial coherence increases with increasing defocus aberration for a given exit slit aperture size and dispersion parameter $\hat{p}$. The increased size of the photon beam at the plane of the exit slit aperture due to defocus aberration leads to a stronger clipping of the photon beam and thus to a higher degree of transverse coherence as expected. Consequently, the effect of defocus aberration favours the spatial coherence properties of the photon beam after the exit slit. At the same time, however, the resolving power is reduced. This is similar to the case without defocus aberration.

4. Discussion

The mathematical description of the interaction of undulator radiation with a grating and the spatial coherence degradation caused by dispersion has been described in the previous sections in the $\{x, \omega\}$ domain. There is a one-to-one correspondence between the $\{x, \omega\}$ and the $\{x, t\}$ domains. This means that the effect of spatial coherence degradation can also be described in the

Optics EXPRESS

$\{x, t\}$ domain. It has been shown that the diffracted field after the grating has an additional phase factor in the $\{x, \omega\}$ domain (Eqs. (28), (27)). In the $\{x, t\}$ domain, the diffracted field contains an additional shift $t - px$. This electric field is described by

$$E_g(x,t) = \frac{1}{2\pi}\int_{-\infty}^{\infty} E_i(\Delta\omega)E_i(x)e^{ip\Delta\omega x}e^{-i\omega t}d\Delta\omega \approx E_i(t-px)E_i(x)e^{-i\omega_0 t}. \tag{61}$$

From Eq. (61) it follows that the temporal field now also spatially dependent, which is known as pulse front tilt phenomenon (PFT) [43–47], i.e., the space and time domains are coupled (space-frequency coupling in the $\{x, \omega\}$ domain).

Prior to the interaction of the undulator radiation with the grating, we assumed only one spatial mode, which implies full spatial coherence of the photon beam (see Eq. (26) and Fig. 7). However, due to the properties of synchrotron undulator radiation, it has a large number of longitudinal or spectral modes (see Fig. 1), implying low temporal coherence. The number of these modes can be estimated from the intensity fluctuations of the undulator radiation (roughly equal to the number of spikes, see Fig. 1). The dispersion effect of the grating leads to a redistribution of the total number of modes, whereby temporal (or spectral) modes are partially converted into spatial modes, resulting in the phenomenon of PFT (see Fig. 7). The degree of redistribution is determined by the dispersion parameter p. In this case the effect of the time delay of a pulse in the dispersion plane is observed for individual temporal modes of the undulator radiation, while each individual mode is spatially fully coherent. The result is multiple spatial modes observed in the dispersion plane for a given bandwidth, statistically causing the decoherence effect.

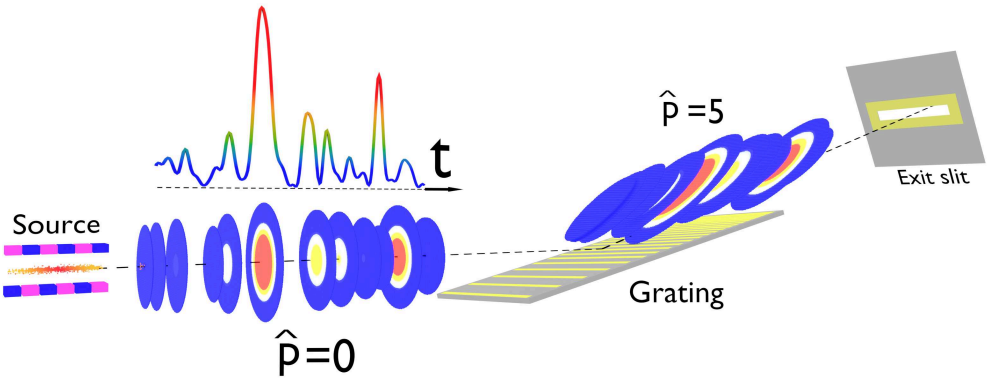

Fig. 7. Visual representation of the SR pulse intensity in the $\{\mathbf{r}, t\}$-domain before and after the interaction with a grating, where normalized dispersion parameter of the pulse with PFT $\hat{p} = 5$.

The statistical analysis presented applies under the assumption that the grating monochromator is unable to resolve individual spectral spikes. If the grating has specifications high enough to resolve individual spectral spikes, the redistribution of modes after the grating would result in a complete conversion of spectral modes into spatial. In this case, only one longitudinal coherence mode would be present and the photon beam would be fully spatially incoherent.

5. Conclusion

The presented analysis shows that a grating used for grating monochromators significantly affects the spatial coherence properties of the photon beam. This effect can be attributed to the properties of synchrotron radiation pulses in combination with the dispersion properties of the grating. It has been shown that the higher the dispersion parameter $\hat{p}$ of the grating, the lower the spatial

Optics EXPRESS

coherence of the diffracted field. The dispersion parameter $\hat{p}$ depends on both the photon energy and the bandwidth of the incident radiation, as well as the footprint of the beam on the grating, its line density and the used diffraction order. Strong dispersion can result in substantially lower values of spatial degree of coherence than those expected in soft X-rays, especially for diffraction-limited synchrotron sources.

It has been shown that the reduced degree of spatial coherence of the diffracted field after the grating is maintained upon propagation and focusing. This is due to the fact that as the beam propagates, only the scales change, not the phase dependencies. In the focal plane, the phase tilt is cancelled for each individual frequency component, but the individual beams are strongly spatially separated, which strongly affects the spatial coherence.

The effects of grating dispersion on the spatial coherence and resolution of the monochromator have been investigated in conjunction with the exit slit aperture. It is shown that the resolving power of the monochromator and the spatial coherence of the dispersed beam can be significantly increased by closing the exit slit. However, it has also been shown that for a given exit slit aperture opening, the degree of spatial coherence is inversely proportional to the resolving power of the monochromator. This means that after passing through the monochromator a highly dispersed beam will have the lowest spatial coherence.

Defocus aberration alone cannot affect the spatial coherence of the photon beam. However, in combination with the monochromator exit slit aperture, it can. The aberration defocuses the photon beam, resulting in over-illumination of the exit slit aperture for a given exit slit aperture size. This results in an increase in spatial coherence and a decrease in the resolving power of the grating.

The presented results can help in mitigating the impact of spatial coherence degradation at synchrotron beamlines that employ grating monochromators. This can be achieved by selecting appropriate grating parameters and settings.

It is important to note, as the result of this analysis, one can see that the effect of spatial coherence degradation is not only associated with the use of grating monochromators, but can also occur with other dispersive optical elements that could potentially be installed at synchrotron facilities, both in the soft and hard X-ray range. Indeed, since spatio-temporal or spatio-frequency coupling and dispersion are inseparable effects, any manifestation of the latter inevitably leads to a degradation of spatial coherence. Such an effect of spatial coherence degradation, even if less pronounced, can potentially be observed, for example by using asymmetrically cut crystals [48].

It would be of great interest to investigate the degradation of spatial coherence caused by a grating for partially coherent X-ray beams at future 4GSRs, which are expected to provide high spatial coherence of the source. This case goes beyond the ideal model considered in this work and imposes complications on the functional forms of the spatial correlation functions. It is expected that the effect of spatial coherence degradation will become even more pronounced than in the ideal case of a fully spatially coherent source. The analysis of the spatial coherence degradation of a grating illuminated by a partially spatially coherent beam will be described in a forthcoming paper.

Acknowledgment. We thank Ivan A. Vartanyants for his interest in this work and Wojciech Roseker for careful reading of the manuscript.

Disclosures. The authors declare no conflicts of interest.

Data availability. Data underlying the results presented in this paper may be obtained from the authors upon reasonable request.

Supplemental document. See Supplement 1 for supporting content.

References

1. P. F. Tavares, S. C. Leemann, M. Sjöström, *et al.*, "The max iv storage ring project," J. Synchrotron Rad. **21**(5), 862–877 (2014).

Optics EXPRESS

2. E. Weckert, "The potential of future light sources to explore the structure and function of matter," IUCrJ **2**(2), 230–245 (2015).
3. C. G. Schroer, I. Agapov, W. Brefeld, *et al.*, "PETRA IV: the ultralow-emittance source project at DESY," J. Synchrotron Rad. **25**(5), 1277–1290 (2018).
4. A. Rodrigues, F. Arroyo, O. Bagnato, *et al.*, "Sirius light source status report," in *Proc. IPAC'18* pp. 2886–2889 (2018).
5. C. G. Schroer, *PETRA IV: upgrade of PETRA III to the Ultimate 3D X-ray microscope. Conceptual Design Report* (Deutsches Elektronen-Synchrotron DESY, 2019).
6. G. Geloni, S. Serkez, R. Khubbutdinov, *et al.*, "Effects of energy spread on brightness and coherence of undulator sources," J. Synchrotron Radiat. **25**(5), 1335–1345 (2018).
7. R. Khubbutdinov, A. P. Menushenkov, and I. A. Vartanyants, "Coherence properties of the high-energy fourth-generation x-ray synchrotron sources," J. Synchrotron Radiat. **26**(6), 1851–1862 (2019).
8. P. Li, M. Allain, T. A. Grünewald, *et al.*, "4th generation synchrotron source boosts crystalline imaging at the nanoscale," Light: Sci. Appl. **11**(1), 73 (2022).
9. J. C. da Silva, C. Guilloud, O. Hignette, *et al.*, "Overcoming the challenges of high-energy X-ray ptychography," J. Synchrotron Radiat. **26**(5), 1751–1762 (2019).
10. W. Chévremont, T. Zinn, and T. Narayanan, "Improvement of ultra-small-angle XPCS with the Extremely Brilliant Source," J. Synchrotron Radiat. **31**(1), 65–76 (2024).
11. T. Narayanan, W. Chévremont, and T. Zinn, "Small-angle X-ray scattering in the era of fourth-generation light sources," J. Appl. Crystallogr. **56**(4), 939–946 (2023).
12. S. Berkowicz, S. Das, M. Reiser, *et al.*, "Nanofocused x-ray photon correlation spectroscopy," Phys. Rev. Res. **4**(3), L032012 (2022).
13. F. Lehmkühler, W. Roseker, and G. Grübel, "From femtoseconds to hours–measuring dynamics over 18 orders of magnitude with coherent x-rays," Appl. Sci. **11**(13), 6179 (2021).
14. G. Geloni, E. Saldin, E. Schneidmiller, *et al.*, "Transverse coherence properties of x-ray beams in third-generation synchrotron radiation sources," Nucl. Instrum. Methods Phys. Res., Sect. A **588**(3), 463–493 (2008).
15. A. Singer and I. A. Vartanyants, "Coherence properties of focused x-ray beams at high-brilliance synchrotron sources," J. Synchrotron Rad. **21**(1), 5–15 (2014).
16. G. Geloni, V. Kocharyan, and E. Saldin, "Brightness of synchrotron radiation from undulators and bending magnets," J. Synchrotron Rad. **22**(2), 288–316 (2015).
17. I. A. Vartanyants and A. Singer, *Coherence Properties of Third-Generation Synchrotron Sources and Free-Electron Lasers* (Springer International Publishing, 2020), pp. 987–1029.
18. F. Siewert, J. Buchheim, T. Zeschke, *et al.*, "On the characterization of ultra-precise x-ray optical components: advances and challenges in ex situ metrology," J. Synchrotron Radiat. **21**(5), 968–975 (2014).
19. M. Yabashi, K. Tono, H. Mimura, *et al.*, "Optics for coherent x-ray applications," J. Synchrotron Radiat. **21**(5), 976–985 (2014).
20. Y. Wang, T. Xiao, and H. Xu, "Effect of surface roughness on the spatial coherence of x-ray beams from third-generation synchrotron radiation sources," J. Synchrotron Radiat. **7**(4), 209–214 (2000).
21. X. Meng, X. Shi, Y. Wang, *et al.*, "Mutual optical intensity propagation through non-ideal mirrors," J. Synchrotron Radiat. **24**(5), 954–962 (2017).
22. C.-C. Cheng and M. Raymer, "Propagation of transverse optical coherence in random multiple-scattering media," Phys. Rev. A **62**(2), 023811 (2000).
23. I. Robinson, C. Kenney-Benson, and I. Vartanyants, "Sources of decoherence in beamline optics," Phys. B **336**(1-2), 56–62 (2003).
24. W. Grizolli, X. Shi, and L. Assoufid, "Influence of optics vibration on synchrotron beam coherence," Opt. Lett. **44**(4), 899–902 (2019).
25. S. Goto, "Effect of beamline optics vibration on the source size and divergence for synchrotron radiation," in *Advances in X-Ray/EUV Optics and Components X*, vol. 9588 (SPIE, 2015), pp. 62–67.
26. K. Bagschik, J. Wagner, R. Buß, *et al.*, "Direct 2D spatial-coherence determination using the Fourier-analysis method: multi-parameter characterization of the *P*04 beamline at PETRA III," Opt. Express **28**(5), 7282–7300 (2020).
27. K. Bagschik, M. Schneider, J. Wagner, *et al.*, "Enabling time-resolved 2d spatial-coherence measurements using the fourier-analysis method with an integrated curved-grating beam monitor," Opt. Lett. **45**(19), 5591–5594 (2020).
28. R. Khubbutdinov, M. Seyrich, and K. Bagschik, "Soft x-ray grating monochromators as a source of spatial coherence degradation: A wave-optical approach," in *Journal of Physics: Conference Series*, vol. 2380 (2022), p. 012072.
29. P. Skopintsev, A. Singer, J. Bach, *et al.*, "Characterization of spatial coherence of synchrotron radiation with non-redundant arrays of apertures," J. Synchrotron Rad. **21**(4), 722–728 (2014).
30. M. Rose, P. Skopintsev, D. Dzhigaev, *et al.*, "Water window ptychographic imaging with characterized coherent X-rays," J. Synchrotron Radiat. **22**(3), 819–827 (2015).
31. L. Mandel and E. Wolf, *Optical Coherence and Quantum Optics* (Cambridge University Press, 1995).
32. J. D. Jackson, *Classical electrodynamics* (John Wiley & Sons, 2021).
33. D. F. Alferov, Y. A. Bashmakov, and P. A. Cherenkov, "Radiation from relativistic electrons in a magnetic undulator," Sov. Phys. Uspekhi **32**(3), 200–227 (1989).
34. H. Onuki and P. Elleaume, *Undulators, Wigglers and their Applications* (CRC Press, 2002).

Optics EXPRESS

35. A. Trebushinin, G. Geloni, Y. Rakshun, *et al.*, "Gaussian random field generator for simulating partially coherent undulator radiation," Optica **9**(8), 842–852 (2022).
36. O. Chubar, G. Williams, Y. Gao, *et al.*, "Physical optics simulations for synchrotron radiation sources," J. Opt. Soc. Am. A **39**(12), C240–C252 (2022).
37. M. Born and E. Wolf, *Principles of Optics: Electromagnetic Theory of Propagation, Interference and Diffraction of Light* (Cambridge University Press, 1999).
38. J. W. Goodman, *Statistical Optics* (Wiley, 1985).
39. I. A. Vartanyants and A. Singer, "Coherence properties of hard x-ray synchrotron sources and x-ray free-electron lasers," New J. Phys. **12**(3), 035004 (2010).
40. S. Serkez, G. Geloni, V. Kocharyan, *et al.*, "Grating monochromator for soft x-ray self-seeding the european xfel," arXiv (2013).
41. I. A. Vartanyants and R. Khubbutdinov, "Theoretical analysis of Hanbury Brown and Twiss interferometry at soft-x-ray free-electron lasers," Phys. Rev. A **104**(2), 023508 (2021).
42. K. Klementiev and R. Chernikov, "Powerful scriptable ray tracing package xrt," in *Advances in computational methods for X-ray optics III*, vol. 9209 (2014), pp. 60–75.
43. E. Treacy, "Optical pulse compression with diffraction gratings," IEEE J. Quantum Electron. **5**(9), 454–458 (1969).
44. Z. Bor, B. Racz, G. Szabo, *et al.*, "Femtosecond pulse front tilt caused by angular dispersion," Opt. Eng. **32**(10), 2501–2504 (1993).
45. J. Hebling, "Derivation of the pulse front tilt caused by angular dispersion," Opt. Quantum Electron. **28**(12), 1759–1763 (1996).
46. S. Akturk, X. Gu, P. Gabolde, *et al.*, "The general theory of first-order spatio-temporal distortions of gaussian pulses and beams," Opt. Express **13**(21), 8642–8661 (2005).
47. A. M. Weiner, *Ultrafast optics* (John Wiley & Sons, 2011).
48. A. Souvorov, M. Drakopoulos, I. Snigireva, *et al.*, "Asymmetrically cut crystals as optical elements for coherent x-ray beam conditioning," J. Phys. D: Appl. Phys. **32**(10A), A184–A192 (1999).